

Cosmic ray transport in Starburst Galaxies and possible observables

Enrico Peretti*^{ab}, Giovanni Morlino^{ca}, Pasquale Blasi^{ab} and Felix Aharonian^{dea}

^a *Gran Sasso Science Institute, Viale F. Crispi 7, 67100, L'Aquila, Italy*

^b *INFN/Laboratori Nazionali del Gran Sasso, via G. Acitelli 22, 67100, Assergi (AQ), Italy*

^c *INAF, Osservatorio Astrofisico di Arcetri, L.go E. Fermi 5, Firenze, Italy*

^d *Max-Planck-Institut für Kernphysik, Postfach 103980, D-69029 Heidelberg, Germany*

^e *Dublin Institute for Advanced Studies, 31 Fitzwilliam Place, Dublin 2, Ireland*

E-mail: enrico.peretti@gssi.it, morlino@arcetri.astro.it,
pasquale.blasi@gssi.it, felix.aharonian@mpi-hd.mpg.de

The nuclei of starburst galaxies are unique sources of high-energy radiation where ideal conditions for cosmic ray acceleration and confinement might be achieved. We investigate the conditions for effective cosmic ray confinement by modelling the transport accounting for diffusion and advection, and we study the implications of such confinement in terms of multifrequency emission and production of high-energy neutrinos. Both primary and secondary electrons, as well as electron-positron pairs produced by gamma ray absorption inside these regions are taken into account. Electrons and positrons produced as secondary products of hadronic interactions are found to be responsible for most of the emission of leptonic origin. In particular, secondary electrons produce an extended synchrotron emission of hard X-rays that represent a remarkable signature of hadronic processes, potentially accessible to current and future observations in the X-ray band. We also apply for the first time our detailed model to study the starburst contribution to the diffuse gamma-ray and neutrino fluxes observed by Fermi-LAT and IceCube. In order to assess such contribution we adopt a redshift number density of starburst-like objects based on the infrared luminosity function inferred by Herschel observations and we take into account the effect of the electromagnetic cascade in the intergalactic medium.

*36th International Cosmic Ray Conference -ICRC2019-
July 24th - August 1st, 2019
Madison, WI, U.S.A.*

*Speaker.

1. Introduction

Ideal conditions for cosmic ray acceleration are expected in the nuclear regions of starburst galaxies (SBGs) where a high supernova rate is observed. These star forming regions, known as starburst nuclei (SBNi), occupy typically the central region of their host galaxies and are highly fragmented in compact star clusters and clouds both embedded in a highly pressurized and hot diluted medium [2]. Due to the large number of supernovae (SNe) and the high level of turbulence, starburst environments are promising for the confinement of particles (see e.g. [11]). Energy losses are expected to be important for both protons and electrons because of the high average target density of the interstellar medium (ISM) and the high inferred magnetic field and radiation field energy densities. The intense star forming activity and high SN rate lead to the launching of a multiphase wind (see [2]) in turn leading to the escape of particles from the SBN where the high level of turbulence might slow down the diffusion.

In such compact and perturbed environment, a leaky-box approach can be adopted. Following the approach developed in [1] (hereafter P19), we model the transport equation as:

$$q(p) = \frac{f(p)}{\tau_{\text{loss}}(p)} + \frac{f(p)}{\tau_{\text{adv}}(p)} + \frac{f(p)}{\tau_{\text{diff}}(p)} = \frac{f(p)}{\tau_c(p)}, \quad (1.1)$$

where f is the CR distribution function, q is the injection term, τ_{loss} , τ_{adv} and τ_{diff} are the timescales of energy losses, advection and diffusion respectively, and $\tau_c^{-1} = \tau_{\text{loss}}^{-1} + \tau_{\text{adv}}^{-1} + \tau_{\text{diff}}^{-1}$ is the compound timescale. The CR injection term for protons is:

$$q_p(p) = \frac{\mathcal{R}_{\text{SN}}}{V_{\text{SBN}}} \mathcal{N}_{\text{inj}}(p), \quad (1.2)$$

where \mathcal{R}_{SN} is the supernova rate, V_{SBN} is the volume of the SBN and \mathcal{N}_{inj} is the injected spectrum. For both protons and electrons we assume the same power-law injection slope in momentum α and high-energy exponential cut-off $p_{p,\text{max}}$ and $p_{e,\text{max}}$ respectively and, as we did in P19, we assume 10^2 PeV c^{-1} for the former and 10 TeV c^{-1} for the latter. We normalize the proton injection function by assuming that a fraction $\xi_{\text{CR}} = 0.1$ of the supernova energy $E_{\text{SN}} = 10^{51} \text{ erg}$ is converted into kinetic energy $T(p)$ of particles:

$$\xi_{\text{CR}} E_{\text{SN}} = \int 4\pi p^2 T(p) \mathcal{N}_{\text{inj}}(p) dp. \quad (1.3)$$

The injection of electrons is directly computed from the protons by assuming a proton-to-electron ratio $q_p/q_e = 50$.

Energy losses of particles are taken into account considering pp interaction, ionization and Coulomb collisions for protons; bremsstrahlung (BREM), synchrotron (SYN), inverse Compton (IC) and ionization for electrons. The advection timescale from the SBN is computed as $\tau_{\text{adv}} = R/v_{\text{wind}}$, where R is the SBN radius and v_{wind} is the wind speed. Similarly we define the timescale of diffusion as $\tau_{\text{diff}}(p) = R^2/D(p)$, where $D(p)$ is the diffusion coefficient that we compute adopting an expression inspired by the quasi-linear formalism:

$$D(p) = \frac{r_L(p)v(p)}{3\mathcal{F}(k)}, \quad (1.4)$$

$D_L(\text{Mpc})$	$\mathcal{R}_{\text{SN}}(\text{yr}^{-1})$	$R(\text{pc})$	α	$B(\mu\text{G})$	$v_{\text{wind}}(\frac{\text{km}}{\text{s}})$	$n_{\text{ISM}}(\text{cm}^{-3})$	$U_{\text{RAD}}(\frac{\text{eV}}{\text{cm}^3})$
3.8	0.05	200	4.25	200	500	125	3400

Table 1: Parameters of typical SBN. In order: 1) luminosity distance, 2) supernova rate, 3) SBN radius, 4) injection index, 5) mean magnetic field, 6) wind speed, 7) ISM density, 8) radiation field energy density from FIR to OPT.

where $\mathcal{F}(k) \propto k^{d-1}$ and it is normalized by assuming $\eta_B = \int_{k_0}^{\infty} \mathcal{F}(k) d \log k$. We accounted for three possible diffusion scenarios: Model A) Kolmogorov spectrum $d = 5/3$ with high level of turbulence $\eta_B \approx 1$ and $L_0 = k_0^{-1} = 1\text{pc}$; Model B) Bohm diffusion, where $\mathcal{F}(k) = 1$ on every scale; Model C) Kolmogorov spectrum with same injection length L_0 of Model A but considering a lower level of turbulence, $\eta_B \ll 1$, such that $D(p)$ has a value comparable to the one in our Galaxy, namely $D(10\text{GeV}/c) = 3 \times 10^{28} \text{cm}^2 \text{s}^{-1}$.

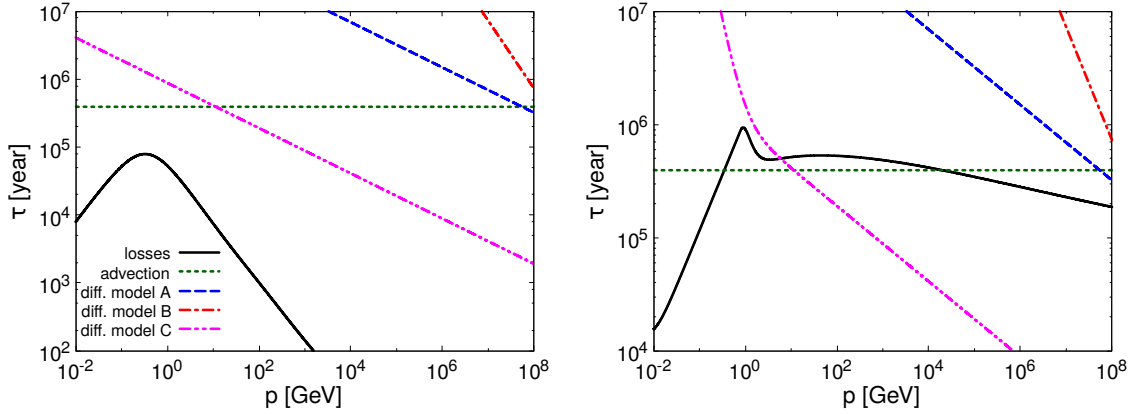


Figure 1: Energy dependence of the characteristic timescales (expressed in years) of cosmic ray electrons (left panel) and protons (right panel) for the parameters of Tab. 1. Black thick lines represent energy losses, green dotted lines show the advection timescales. The timescales of diffusion are represented by blue dashed lines in the case of Model A, red dot-dashed in the case of Model B and magenta dot-dot-dashed in the Model C.

We show in Fig. 1 the timescale of electrons (left panel) and protons (right panel) in SBNi for a set of parameters typical of SBNi (see Tab. 1). While electrons are loss-dominated for a typical wind speed and for all diffusion models, the case of protons is a priori less clear. In fact, the advection and the loss timescale are comparable at all relativistic energies. Moreover, in the diffusion Model C, relativistic protons diffuse away from the SBN before losing their energy.

During their transport high-energy protons collide with particles of the ISM producing π^0 and π^\pm which decay respectively into gamma-rays and electrons (we call electrons both e^- and e^+) and neutrinos, and we compute their spectra following [3]. The rate of injection of secondary electrons is computed as:

$$q_{e,\text{sec}}(p) \approx 2 \frac{n_{\text{ISM}} \sigma_{pp} c}{\kappa^3} f_p(p/\kappa) = 2\eta \kappa^{\alpha-3} q_p(p) \quad (1.5)$$

where n_{ISM} is the ISM density, $\sigma_{pp} \approx 50\text{mb}$ is the pp cross section, $\kappa \approx 1/20$ is the inelasticity and $\eta = \tau_c / (n_{\text{ISM}} \sigma_{pp} c)^{-1}$ is the ratio between the proton compound timescale and the typical

pp -interaction timescale, which measures the level of calorimetry of the source: it is energy independent if transport is dominated by advection.

Due to the strong infrared background photon field, SBNi are expected to be opaque to very-high-energy gamma rays. These absorbed gamma rays produce electron-positron pairs which lose almost immediately their energy via SYN and IC. The rate of injection of pairs, (here referred to as *tertiaries*) is computed as:

$$q_{e,\text{ter}}(p) \approx \frac{n_\gamma(pc) \tilde{\tau}_{\gamma\gamma}(pc) c^2}{4\pi p^2 R} \approx \frac{(R/c) n_{\text{ISM}} \sigma_{pp} c f_p(pc/\tilde{\kappa}) \tilde{\tau}_{\gamma\gamma}(pc) c^2}{\tilde{\kappa}} = \tilde{\tau}_{\gamma\gamma}(pc) \eta \tilde{\kappa}^{\alpha-3} q_p(p) \quad (1.6)$$

where $n_\gamma(E)$ is the gamma-ray number density per unit energy assumed to be dominated by the π^0 component, $\tilde{\kappa} \approx 1/10$ is the inelasticity and $\tilde{\tau}_{\gamma\gamma} = \text{Min}[\tau_{\gamma\gamma}, 1]$. Tertiary particles are injected above a threshold in energy but during their transport they cool down populating also energies below the threshold.

2. Hard X-rays as a marker of hadronic interactions

The secondary-to-primary electrons ratio \mathcal{R}_{sp} carries precious information on the confinement of protons. In particular, if $\tau_{\text{adv}} \ll \tau_{\text{diff}}$, according to Eq. (1.5) we have:

$$\mathcal{R}_{sp} = \frac{f_{e,\text{sec}}(p)}{f_{e,\text{prim}}(p)} = \frac{q_{pp \rightarrow e}(p)}{q_e(p)} \approx \frac{2\eta \kappa^{\alpha-3} q_p(p)}{q_p(p)/50} = 10^2 \eta \kappa^{\alpha-3}. \quad (2.1)$$

On the other hand, if the transport of protons is diffusion-dominated, the spectrum of secondaries is softer than that of primaries (see left panel of Fig. (2)) and \mathcal{R}_{sp} is no longer energy-independent. Similarly, the tertiary-to-secondary ratio \mathcal{R}_{ts} is tightly linked to the gamma-ray optical depth. Assuming again $\tau_{\text{adv}} \ll \tau_{\text{diff}}$ and using Eq. (1.5) and Eq. (1.6) \mathcal{R}_{ts} reads

$$\mathcal{R}_{ts} = \frac{f_{e,\text{ter}}(p)}{f_{e,\text{sec}}(p)} = \frac{q_{\gamma\gamma \rightarrow e}(p)}{q_{pp \rightarrow e}(p)} \approx \frac{\tilde{\tau}_{\gamma\gamma} \eta \tilde{\kappa}^{\alpha-3} q_p(p)}{2\eta \kappa^{\alpha-3} q_p(p)} = \frac{\tilde{\tau}_{\gamma\gamma}}{2} \left(\frac{\tilde{\kappa}}{\kappa}\right)^{\alpha-3}. \quad (2.2)$$

Both \mathcal{R}_{sp} and \mathcal{R}_{ts} can be $\gtrsim 1$ and, differently from primaries, secondary and tertiaries are constantly produced with energies larger than ~ 10 TeV. The presence of electrons up to PeV energies and the high values of both U_B and U_{RAD} are expected to produce an enhanced hard X-ray flux via SYN and IC. The hot thermal bath permeating SBNi is inferred to be $\lesssim 10^7$ K, therefore a diffuse emission at energies larger than a few keV can be produced only by non-thermal processes (see also [10]). Fig. 2 compares the particle (left panel) and high energy photon (right panel) spectra obtained with diffusion model A (model B gives practically the same results) and model C for the same set of parameters used in Fig. 1. While primary electrons and their emissivity are the same for both models, protons and their byproducts strongly reflect the different diffusion scenarios. In particular, primary protons maintain their injection slope in model A, whereas they steepen in model C; this difference reflects in the π^0 component of the photon spectra. Similarly, diffusion affects also secondaries and tertiaries which in turn modify the expected flux in hard X-rays; more specifically we observe a factor ~ 3 difference in the flux at ~ 10 keV. The two vertical lines in the left panel helps to quantify the difference in the expected hard X-rays. They label the energies at which electrons radiate at ~ 10 keV via SYN (mostly secondaries and tertiaries

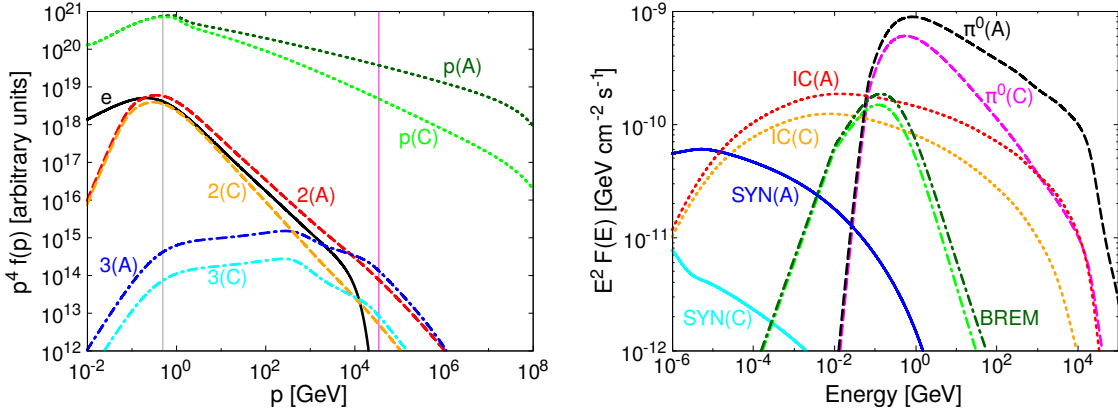


Figure 2: Left panel: Particle spectra for different diffusion model A and C. Dotted lines represent protons (p), dashed lines secondaries (2), dot-dashed tertiaries (3) and the thick black line primary electrons (e) for both diffusion scenarios. The two vertical lines represent the energies at which electrons are radiating at ~ 10 keV via SYN (magenta) and IC (grey). Right panel: comparison of the multiwavelength high-energy spectra decomposed in the various components for the same diffusion model A and C. Dashed lines represent the π^0 component, dotted inverse Compton (IC), thick synchrotron (SYN) and dot-dashed bremsstrahlung (BREM).

at ~ 35 TeV) and IC (primaries and secondaries at ~ 0.5 GeV on FIR photons). They show in particular a small modification of secondaries at GeV (where tertiaries are irrelevant) and an order of magnitude difference at multi-TeV energies. As for electrons, while the IC flux changes by about $\sim 20 - 30\%$, the SYN flux increases by about an order of magnitude. The simultaneous presence of high hard X-ray luminosity and a hard slope in the gamma-ray spectrum would suggest that efficient confinement is reached in a SBN.

3. Diffuse neutrino flux from highly star forming galaxies - M82 prototype

The opacity to very-high-energy gamma rays together with the promising confinement conditions for CR protons make SBNi ideal neutrino emitters. On the other hand, the sensitivity of current neutrino observatories is still more than one order of magnitude lower than what is required to observe the nearest starbursts like NGC253 or M82. In the perspective of a possible detection of starbursts in the neutrino channel, the lack of a sufficiently high neutrino luminosity is compensated by the high number of SBGs expected from the star formation history of the Universe. In particular, their number density inferred for $1 \lesssim z \lesssim 2$ is much higher than what is observed in the local Universe suggesting that they might be observable as a diffuse component. For the source counting we adopt the star formation rate function (SFRF) approach described in [5]:

$$\Phi(\psi, z) d \log \psi = \tilde{\Phi} \left(\frac{\psi}{\tilde{\psi}} \right)^{1-\tilde{\alpha}} \exp \left[-\frac{1}{2\tilde{\sigma}^2} \log^2 \left(1 + \frac{\psi}{\tilde{\psi}} \right) \right] d \log \psi, \quad (3.1)$$

where we fit the free parameters $\tilde{\Phi}$, $\tilde{\psi}$ and $\tilde{\sigma}$ at each redshift interval, and assume $\tilde{\alpha} = 1.6$ based on observations of low redshift SBGs.

Since the SFR (ψ) is an increasing function of the ISM density (see [6]), we expect that the higher the SFR the better a SBN behaves as a proton calorimeter. In particular, when losses

D_L (Mpc)	$\mathcal{R}_{\text{SN}} (\text{yr}^{-1})$	B (μG)	$v_{\text{wind}} (\frac{\text{km}}{\text{s}})$	$n_{\text{ISM}} (\text{cm}^{-3})$	$U_{\text{RAD}} (\frac{\text{eV}}{\text{cm}^3})$	$\Psi_{\text{M82}} (\frac{M_{\odot}}{\text{yr}})$
3.9	0.05	250	700	150	2500	5

Table 2: Parameters of the SBN prototype tuned on M82 multiwavelength spectrum.

dominate, according to Eq. (1.5), the injection of hadronic secondaries depends only on the proton injection, which in turn is proportional to \mathcal{R}_{SN} . For this reason, assuming diffusion model A described in §1, we took M82 as starburst prototype and we assumed that the injected neutrinos and gamma-rays scale linearly with the SFR as

$$q_{\gamma,v}^{\text{SBN}}(E, \psi) = \left(\frac{\psi}{\psi_{\text{M82}}} \right) q_{\gamma,v}^{\text{M82}}(E). \quad (3.2)$$

In the left panel of Fig. 3 we show the spectrum of our SBN prototype tuned to M82 data, where we fixed the injection slope to 4.2 and the radius to 200 pc, whereas the other parameters have been found by fitting M82 spectrum (see Tab. 2).

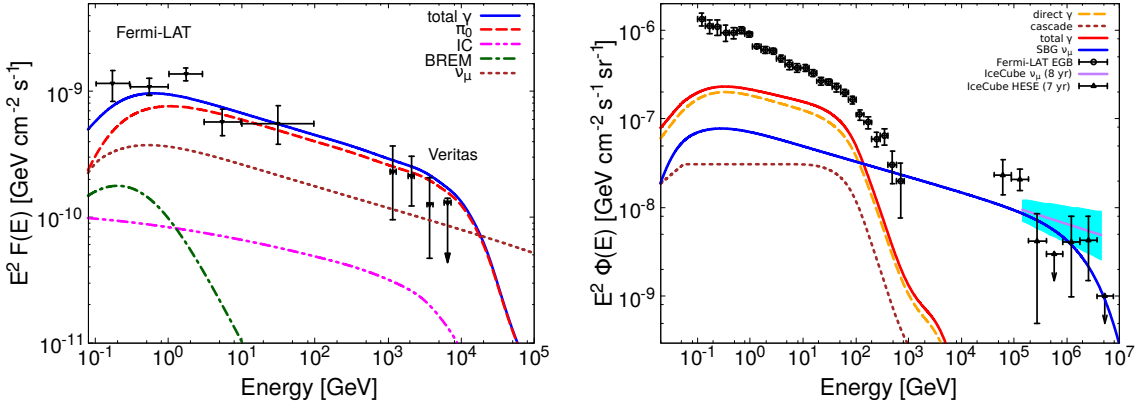


Figure 3: Left panel: gamma-ray (blue thick line) and neutrino (brown dotted line) spectra of the starburst prototype compared with M82 data ([12] and [13]). The contribution of single spectral components are shown separately: hadronic (red dashed), inverse Compton (magenta dot-dot-dashed) and bremsstrahlung (green dot-dashed). Right panel: diffuse gamma-ray (thick red) and single flavor neutrino (thick blue) diffuse fluxes compared with Fermi-LAT (see [15]) and IceCube data (both HESE [14] and trough-going muons [16]). The contribution of direct gamma-rays (orange dashed) and the cascade (brown dotted) are shown separately.

We compute the diffuse gamma-ray and neutrino spectra integrating the emitted flux over cosmological history:

$$\Phi_{\gamma,v}(E) = \frac{1}{4\pi} \int_0^{4.2} dz \frac{dV_C}{dz} \int_{\psi_{\text{min}}} d \log \psi \Phi_{\text{SFR}}(\psi, z) [1+z]^2 f_{\gamma,v}(E[1+z], \psi) \quad (3.3)$$

where dV_C/dz is the standard comoving volume element, the term $df_{\gamma,v}(E, \psi) = dN(E)/dt dS dE$ is the flux computed according to Eq. (3.2) which scales with $(1+z)^2$ and $\psi_{\text{min}} \sim 1 M_{\odot} \text{yr}^{-1}$ has been estimated requiring the source to be at least partially calorimetric, $\tau_{\text{loss}} \sim \tau_{\text{adv}}$. Below such threshold CRs are not efficiently confined and secondary production is strongly reduced.

Gamma rays propagating from their source to the Earth interact with the extragalactic background light (EBL) and cosmic microwave background (CMB) and are highly absorbed and reprocessed at lower energies via pair production on low energy EBL+CMB photons and IC of these pairs on the same low energy background. The latter process is known as electromagnetic cascade and it has a universal spectral feature. We take it into account following the analytic approach developed in [4] assuming a fixed comoving EBL peak at the energy of ~ 1 eV. The gamma-ray opacity of the EBL+CMB has been taken from [7]. The right panel of Fig. 3 shows the result of Eq. (3.3) where we are consistent with the 1σ upper limit of the Fermi-LAT non-blazar contribution of gamma-rays for energies > 50 GeV [8], roughly $\sim 40\%$ of the extragalactic gamma-ray background. In particular, we found that the gamma-gamma absorption at TeV energies inside each starburst is important for a correct estimate of the EGB in the > 50 GeV energy band because it lowers the energy content of the electromagnetic cascade. In conclusion, as one can see from Fig. 3 our model can account for the neutrino flux above ~ 200 TeV, whereas it under-predicts the flux at lower energies (see also [9]). Despite the large number of SBGs expected at $z \gtrsim 1$, the percentage of the observed diffuse neutrino flux explainable with SBGs might change if one considers different assumptions on the injection slope α , the maximum momentum $p_{p,\max}$ or the astrophysical uncertainty on ψ_{M82} . A detailed analysis of the impact of these parameters goes beyond the goals of this proceeding and we leave it for an upcoming paper in preparation.

4. Conclusions

We developed a self-consistent model able to compute the stationary solution of the transport equation for protons and electrons and their associate multiwavelength photon and neutrino emission. We investigated how different assumption on the diffusion coefficient can possibly change the confinement condition. Assuming a level of turbulence quantified by $\eta_B \approx 1$ the proton calorimetry is at least partially achieved, whereas calorimetric condition for electrons are expected to be fully reached in all realistic diffusion scenarios. The quasi-achieved proton calorimetry is expected to result in a high-energy gamma-ray spectrum dominated by photons of hadronic origin which maintain the slope of their parent protons and suffer a strong absorption above a few TeV by the thermal background. Together with hadronic gamma rays, secondary electrons and pairs are also expected to be copiously produced up to \sim PeV energies and emit intense radiation at hard X-ray frequencies which might be detected by current operating satellites. Such enhanced non-thermal hard X-ray flux can be interpreted as smoking gun for hadronic processes taking place in starburst environment and help us in understanding the actual diffusion scenario in these regions.

We tuned our SBN model to obtain a prototype source and we computed the starburst nuclei distribution in redshift adopting the star formation rate function approach. Accounting for the effects of the electromagnetic cascade in the intergalactic medium we computed the diffuse gamma-ray and neutrino flux of starburst origin. We showed that the gamma-gamma absorption inside the starbursts plays an important role in lowering the energy content of the electromagnetic cascade and we have found that starburst nuclei could explain the neutrino flux observed by IceCube above 200 TeV without exceeding gamma-ray constraints. On the other hand below such energy, another contribution is required, which could be due to another class of astrophysical sources or to a contamination of atmospheric neutrinos. In conclusion, two arguments would support efficient

cosmic ray confinement in SBNi: 1) enhanced hard X-rays flux associated with a hard slope in the gamma-ray spectrum; 2) a contribution from SBNi to the diffuse neutrino flux.

References

- [1] E. Peretti, P. Blasi, F. Aharonian and G. Morlino, *Cosmic ray transport and radiative processes in nuclei of starburst galaxies*, *MNRAS* **487** (2019) 168 [astro-ph.HE/1812.01996].
- [2] M.S. Westmoquette et al., *The Optical Structure of the Starburst Galaxy M82. II. Nebular Properties of the Disk and Inner-Wind*, *APJ* **706** (2009) 1571 [astro-ph.CO/0907.3162].
- [3] S.R. Kelner et al., *Energy spectra of gamma rays, electrons, and neutrinos produced at proton-proton interactions in the very high energy regime*, *PRD* **74** (2006) 034018 [astro-ph/0606058].
- [4] V. Berezhinsky and O. Kalashev, *High-energy electromagnetic cascades in extragalactic space: Physics and features*, *PRD* **94** (2016) 023007 [astro-ph.HE/1603.03989].
- [5] C. Gruppioni et al., *Star Formation in Herschel's Monsters versus Semi-Analytic Models*, *MNRAS* **451** (2015) 3419 [astro-ph.GA/1506.01518].
- [6] R.C. Kennicutt, *The Global Schmidt Law in Star-forming Galaxies*, *APJ* **498** (1998) 541 [astro-ph/9712213].
- [7] A. Franceschini and G. Rodighiero, *The extragalactic background light revisited and the cosmic photon-photon opacity*, *A & A* **603** (2017) A34 [astro-ph.HE/1705.10256].
- [8] M. Lisanti et al., *Deciphering Contributions to the Extragalactic Gamma-Ray Background from 2 GeV to 2 TeV*, *APJ* **832** (2016) 117 [astro-ph.HE/1606.04101].
- [9] K. Bechtol et al., *Evidence against star-forming galaxies as the dominant source of IceCube neutrinos*, *APJ* **836** (2017) 47 [astro-ph.HE/1511.00688].
- [10] B.C. Lacki and T.A. Thompson, *Diffuse Hard X-ray Emission in Starburst Galaxies as Synchrotron from Very High Energy Electrons*, *APJ* **762** (2013) 29 [astro-ph.HE/1010.3030].
- [11] T.M. Yoast-Hull, J.E. Everett, J.S. Gallagher and E.G. Zweibel, *Winds, Clumps, and Interacting Cosmic Rays in M82*, *APJ* **768** (2013) 53 [astro-ph.HE/1303.4305].
- [12] F. Acero et al. *Fermi Large Area Telescope Third Source Catalog*, *APJ Suppl.* **218** (2015) 23 [astro-ph.HE/1501.02003].
- [13] V.A. Acciari et al., *A connection between star formation activity and cosmic rays in the starburst galaxy M82*, *Nature* **462** (2009) 770 [astro-ph.CO/0911.0873].
- [14] F. Halzen and A. Kheirandish, *Multimessenger Search for the Sources of Cosmic Rays Using Cosmic Neutrinos*, *Front. Astron. Space Sci.* **6** (2019) 32.
- [15] M. Ackermann et al., *The Spectrum of Isotropic Diffuse Gamma-Ray Emission between 100 MeV and 820 GeV*, *APJ* **799** (2015) 86 [astro-ph.HE/1410.3696].
- [16] C. Haack et al., *A measurement of the diffuse astrophysical muon neutrino flux using eight years of IceCube data.*, in proceeding of *ICRC 2017*, [PoS \(ICRC2017\) 1005](#) (2017).

Acknowledgments

The authors are grateful to Pierluigi Monaco and Pierre Cristofari for useful discussion and their precious suggestions.